Understanding the Principles of Co-deposition of Mixed-SAMs in MAPbI3-Based p-i-n Structure Perovskite Solar Cells

Wang, Haoxu; Yan, Jin; Dijkstra, Mare; Torun, Engin; Rana, Moumita; Procel Moya, Paul; Santbergen, Rudi; Zeman, Miro; Isabella, Olindo; Mazzarella, Luana

DOI
10.1021/acsami.5c18266

Publication date
2025

Document Version
Final published version

Published in
ACS Applied Materials and Interfaces

ACS APPLIED MATERIALS & INTERFACES

www.acsami.org

Research Article

Understanding the Principles of Co-deposition of Mixed-SAMs in $MAPbI_3$-Based p-i-n Structure Perovskite Solar Cells

Haoxu Wang,* Jin Yan, Mare Dijkstra, Engin Torun, Moumita Rana, Paul Procel Moya, Rudi Santbergen, Miro Zeman, Olindo Isabella, and Luana Mazzarella*

Cite This: *ACS Appl. Mater. Interfaces* 2025, 17, 67306−67317

Read Online

ACCESS | Metrics & More | Article Recommendations | Supporting Information

ABSTRACT: The integration of self-assembled monolayers (SAMs) in perovskite (PVK) solar cells often presents processing challenges that can hinder their industrial uptake. To address these limitations and enhance the manufacturability of the SAMs/PVK interface, a co-deposition strategy was recently developed, wherein both SAMs and PVK films are formed simultaneously in a single step. As the fundamental principles governing the SAM/PVK co-deposition process remain insufficiently explored, here we selected four commercially available SAMs molecules—MeO-4PACz, Me-4PACz, Me-2PACz, and 2PACz—and we mixed them based on their molecular size, polarity, and hydrophobicity, forming pairs. The co-deposition process of mixed-SAMs with $MAPbI_3$ precursor solutions was studied, and corresponding solar cell devices were fabricated. Among the three combinations tested, the MeO-4PACz + Me-4PACz one yields the most promising results, and a power conversion efficiency of approximately 19% was achieved without any additional passivation strategies. Our findings reveal that the co-deposition process of mixed-SAMs is primarily influenced by the interplay between molecular size and polarity. The binding strength of co-deposited mixed SAMs to the In_2O_3:Sn (ITO) substrate is largely dictated by their solvation behavior in the PVK precursor-DMF:DMSO solvent system. This conclusion is supported by quantum chemistry calculations and further corroborated by surface, structural, and compositional analysis.

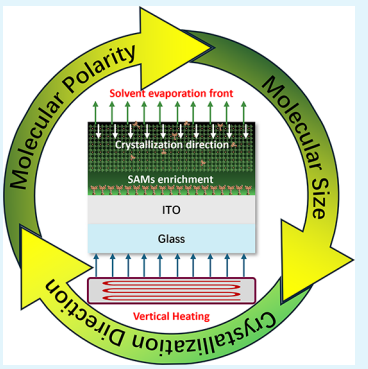

KEYWORDS: *$MAPbI_3$, mixed-SAMs, co-deposition, solvation effect, molar polarity*

INTRODUCTION

Perovskite (PVK) solar cells (PSCs) have achieved outstanding power conversion efficiency (PCE) in both single junction (27%) and tandem devices (34%),[1,2] benefiting from multiple engineering strategies over the past 15 years. Since self-assembled monolayers (SAMs) were first reported for use in PSCs as an alternative to more traditionally used hole transport layers (HTLs), they have been widely praised for facilitating good interfacial contact, excellent energy-level alignment, effective hole extraction, and negligible parasitic absorption losses.[3] The typical structure of SAMs molecules usually consists of 3 parts: the anchoring group, the linker (stem) group, and the head (terminal) group.[4] The anchoring group ($-PO_3H_2$, $-COOH$, $-SO_3H$, $-BO_2H_2$, etc.) facilitates the chemical interactions between SAMs and the substrate or adjacent functional layers such as in combination with other HTL or electron transporting layer (ETL).[5−7] The length of the linker group tunes the width of the tunneling barrier of charge transfer forming at the interface and slightly affects the molecular polarity. It can also regulate the interaction of SAMs molecules during the self-assembly process and their molecular packing. The headgroup mainly controls the dipole moment for finely tuning the energy level and work function (WF) of the target surface. The donor group based on carbazole has been widely deployed and studied as the headgroup for its efficient electron delocalizing effect and effective hole-selective, as well as extraction properties.[8,9]

In the classic p-i-n structure PSC manufacturing, the SAMs solution is directly spin-coated or dip-coated onto the In_2O_3:Sn (ITO)-coated substrate to form the monolayer, followed by the PVK film.[4] However, unresolved challenges remain, such as nonuniform agglomeration on the ITO surface and difficult film formation of the subsequent spin-coated PVK layer due to the hydrophobicity of functional groups. Mixed-SAMs strategies were proposed to improve ITO surface coverage while enhancing ion migration suppression within the PVK absorber.[10−12] The majority of mixed-SAMs studies focus on designing novel additives or synthesizing new SAMs molecules to enhance coverage and tune energy-level structures, improving the limitations of commercially available SAMs.[6,11,13−16] These advances have indeed led to significant progress, although the reliance on custom-synthesized additives or SAMs molecules poses a substantial barrier for

Received: September 12, 2025
Revised: November 17, 2025
Accepted: November 20, 2025
Published: December 1, 2025

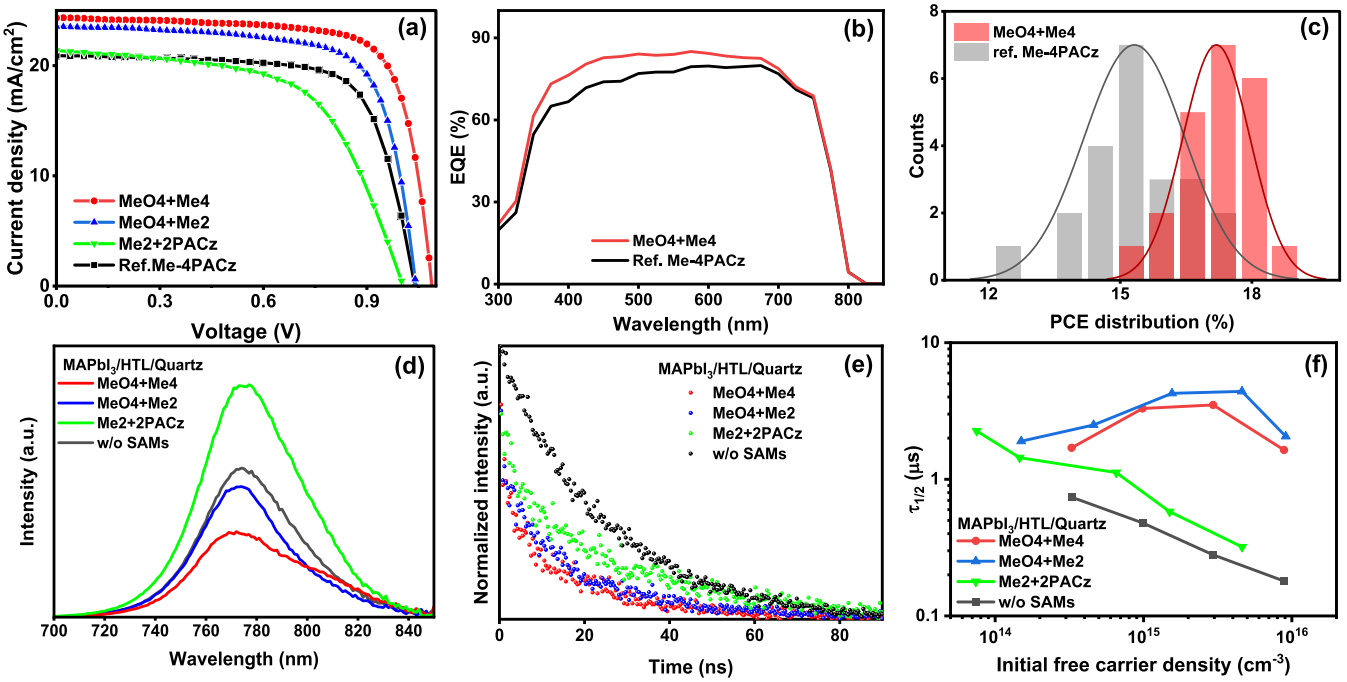

Figure 1. Device performance and material characterizations of co-deposited mixed-SAMs/$MAPbI_3$ and co-deposited Me-4PACz/$MAPbI_3$ (reference): (a) J-V characteristics; (b) EQE spectra; (c) PCE distribution of the PSCs based on different mixed-SAMs; (d) steady-state photoluminescence (SSPL) spectra, (e) time-resolved photoluminescence (TRPL) results, and (f) half-lifetime ($\tau_{1/2}$) of $MAPbI_3$/mixed-SAMs/quartz structures as a function of the initial free carrier density with different combinations of SAMs.

other research teams attempting to replicate these methods.[12] To avoid the hydrophobicity problem caused by methyl groups and improve process simplicity, Zheng et al. first demonstrated a versatile co-deposition method by adding Me-4PACz directly to different PVK precursor solution systems, circumventing the hydrophobic limitations posed by methyl groups.[17] Tan et al. then reported a successful co-deposition method based on dimethylacridine (DMAcPA) molecule added to PVK precursor with a PCE over 25%.[18] Gao et al. recently demonstrated the importance of novel SAMs molecule design (D4PA) in the co-deposition process.[19] The C−C bond coupling in D4PA prevents the molecule agglomeration in PVK precursor and strong bonding to PVK and ITO substrate. Other co-deposition examples were also reported in PVK solar cells, PVK LEDs, and organic photovoltaic devices.[20−22] The co-deposition method exhibits indeed a remarkable versatility, as it is not only compatible with various SAMs (such as 2PACz, Me-4PACz, DMAcPA, D4PA, etc.) but also with solution systems of different PVK components.[20−22]

Despite the successful applications, co-deposition remains not fully explored with limited studies on its specific process and underlying mechanisms. Jing et al. proposed that the introduction of 2PACz into the PM6:Y6-BO bulk heterojunction (BHJ) blend in organic solar cells (OSCs) could trigger the in situ formation of anode interlayer during the crystallization process of the photoactive layer.[23] The self-aggregation of 2PACz on the ITO substrate is attributed to the surface energy difference between 2PACz and the photoactive components.[23,24] Wu and colleagues successfully fabricated a mixed Sn−Pb PSC without an HTL by incorporating 2PACz into the PVK precursor solution.[25] Quantum chemistry calculations indicated that 2PACz has a stronger coordination ability with Sn^{2+}. It was found that 2PACz molecules condense at the grain boundaries or surfaces of the PVK film and especially tend to accumulate at the buried interface between the perovskite film and the ITO substrate, as evidenced by the distinct phosphorus signal. It can be reasonably concluded that this preferential spatial distribution is due to the targeted coordination functionality of 2PACz molecules with Sn ions, which are a key component of the ITO electrode.[25] Tan et al. proposed a molecular-extrusion model to understand the unique distribution of molecules based on DMAcPA.[18] The top-down crystallization of the PVK film is initiated by the evaporation of the solvent during the chlorobenzene (CB) quenching process, where SAMs molecules are speculated to be pushed downward and extruded to the ITO surface.[26] Specifically, during the quenching process, the relatively weak Pb−O coordination between the PVK and DMAcPA dissociates due to the stronger Pb−I bonds, leading to the expulsion of DMAcPA-PbI and the chelation onto the crystal surface.[18] The above studies considered the interactions between SAMs molecules and PVK components, but they do not provide the differences in properties and behavior patterns of different SAMs molecules during the co-deposition process. Additionally, all of these studies are based on single-component SAMs molecules.

In this study, we compared the behavioral differences of SAMs molecules during the co-deposition in PVK films and systematically studied the interactions between the mixed SAMs molecules and the DMF:DMSO solvent system. Based on a comprehensive review of SAMs research, commercially available SAMs molecules were utilized in mixed modifications to improve the poor coverage of single SAM layers. Additionally, a one-step co-deposition method of SAMs and PVK was adopted to simplify preparation and address the hydrophobicity issues inherent in SAMs molecules. Four SAMs molecules, MeO-4PACz, Me-4PACz, Me-2PACz, and 2PACz, were selected, and various combinations were tested in p-i-n

https://doi.org/10.1021/acsami.5c18266
ACS Appl. Mater. Interfaces 2025, 17, 67306−67317

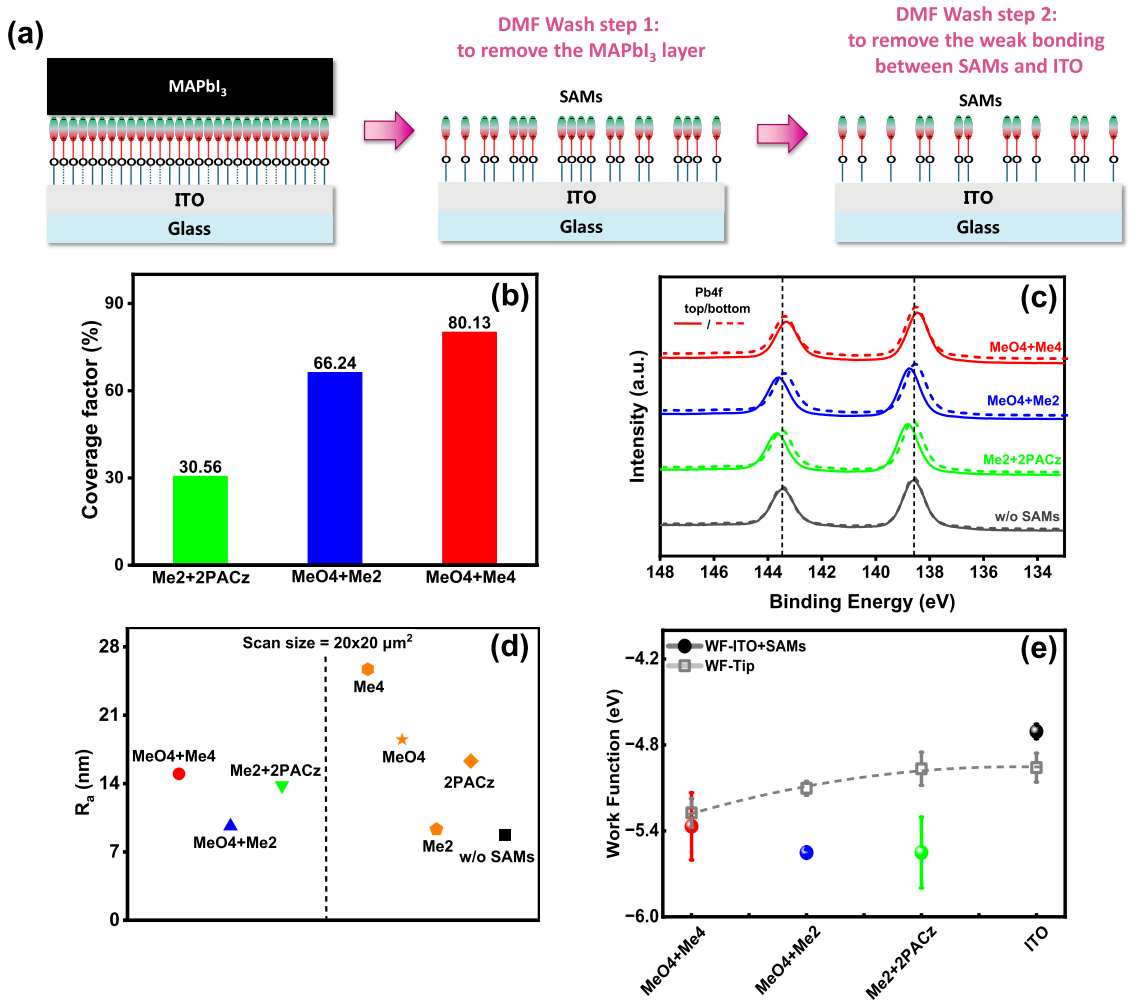

Figure 2. Elemental analysis and coverage of different mixed-SAMs onto ITO substrates. (a) Schematic of DMF wash procedure to remove $MAPbI_3$ layer (step 1) and weakly bonded mixed-SAMs (step 2) from ITO substrate. (b) Coverage factors extracted from the counts per second (cps) ratio of the O 1s peak of different mixed-SAMs on ITO. (c) XPS peak shift of Pb 4f at the top (film side, solid line) and bottom (substrate side, dashed line) surfaces of the $MAPbI_3$ film. XPS peak shifts of I 3d at the top and bottom surfaces of the $MAPbI_3$ film are reported in Figure S10. (d) Extracted surface roughness (R_a) of PVK films co-deposited with mixed-SAMs and single SAM with a scan size of 20 × 20 μm^2. (e) Calculated work function (WF) from Kelvin probe force microscopy (KPFM) measurements of mixed-SAMs/ITO samples.

structured $MAPbI_3$ perovskite solar cells. To assess the effects of SAMs-PVK co-deposition on PVK film, factors such as interfacial contact, energy-level alignment, and SAMs residue in PVK were quantified. The compatibility of the co-deposition approach with different mixed-SAMs combinations was demonstrated, and different coverage and uniformity were observed, which depend on the specific mixed-SAMs selected. The solar cell results confirmed the same trend, in which the narrow distribution of device performances indicates that MeO-4PACz+Me-4PACz mixed SAMs is the optimal combination among the different tested. In the end, the principle of the $MAPbI_3$+mixed-SAMs co-deposition dynamic process was thoroughly analyzed and discussed through quantum chemistry calculations.

RESULTS AND DISCUSSION

Based on the study of Zheng et al., Me-4PACz has already been demonstrated as a universally applicable SAM for co-deposition with different perovskite precursor solution systems.[17] However, they did not further explore or elucidate the underlying reasons for its selection as an optimal candidate. Building upon this, we further introduced Me-2PACz to compare the behavior of SAMs with different molecular sizes in co-deposition. Additionally, MeO-4PACz and 2PACz were incorporated to study the effects of different functional groups on SAMs' behavior during the co-deposition process. We selected three mixed-SAMs combinations: MeO-4PACz+Me-4PACz (MeO4+Me4), MeO-4PACz+Me-2PACz (MeO4+Me2), and Me-2PACz+2PACz (Me2+2PACz) to combine the SAMs with different sizes and different functional groups together and studied the film formation behavior and mechanisms in the co-deposition process using PbI_2 and MAI as PVK precursors to obtain $MAPbI_3$ (Figure S1). We fabricated PSCs applying the mixed-SAMs co-deposition approach to obtain, in a single step, both the HTL and the PVK absorber. The p-i-n device has the following structure: Ag/BCP/$PC_{61}BM$/$MAPbI_3$/mixed-SAMs/ITO (Figure S2). Figure 1a–c shows the device performance of solar cells based on codeposited Me-4PACz (reference) and the codeposited mixed-SAMs as HTL. The J-V curves are depicted in Figure 1a, and the corresponding solar cell parameters of the best devices for each combination tested are reported in Table S1. The mixed-SAMs based on MeO4+Me4 contributes to an

https://doi.org/10.1021/acsami.5c18266
ACS Appl. Mater. Interfaces 2025, 17, 67306–67317

overall improvement of all of the cell parameters with PCE of 18.48%, representing an absolute increase of 2.96% with respect to the reference device, ranking among the top performers in p-i-n $MAPbI_3$ solar cells (see Table S2). The integrated short-circuit current density (J_{sc}) values, derived from external quantum efficiency (EQE) spectra in Figure 1b, are 19 mA/cm^2 for the reference device and 20.5 mA/cm^2 for MeO4+Me4. The EQE curve indicates higher absorption in the wavelength range of 400−700 nm, with slight deviation from the J-V measurements (Table S1). This result indicates that the overall PVK film quality and bottom interface contact of the $MAPbI_3$ layer (illuminated side) are effectively improved by the mixed-SAMs co-deposition. The optimized devices with the MeO4+Me4 combination exhibit a narrow performance distribution and consistent device parameters, resulting in enhanced PCE as shown in Figures 1c and S3. The improved open-circuit voltage (V_{oc}) in Figure 1a can be attributed to better ITO/mixed-SAMs/PVK interfacial contact. Additionally, the enhancement in fill factor (*FF*) by $+3.04\%_{abs}$ is due to reduced leakage current between the PVK/ITO interface due to the vacancy of uncoordinated SAMs.[18]

To address the differences among the different combinations of mixed-SAMs, we investigated the PVK films after the co-deposition process. Figure 1d shows the steady-state photoluminescence (SSPL) spectra of reference $MAPbI_3$ w/o SAMs and three different mixed-SAMs/$MAPbI_3$. All PL spectra are centered at ∼770 nm with different intensities.[27,28] Compared to the reference sample, the PL intensities of MeO4+Me4 and MeO4+Me2 are reduced. This result suggests effective carrier extraction from PVK, which in turn reduces luminescence intensity. Conversely, the sample with Me2+2PACz exhibits a higher PL intensity, indicating compromised carrier extraction and enhanced radiative recombination. Since the methoxyl group (MeO) and phosphoxy group (P═O) in the SAM molecule can effectively passivate the PVK layer, the increased PL intensity could be attributed to the nonoriented distribution of Me2+2PACz (green spectrum in Figure 1d) within the $MAPbI_3$.[29,30] In Figure 1e, time-resolved photoluminescence (TRPL) spectra show a progressively faster decay in time with the addition of mixed-SAMs compared to the reference $MAPbI_3$. Table S3 lists the average lifetimes (τ_{ave}) of each sample. Consistently, both PL and TRPL results align with the device performance shown in Figure 1a as previously mentioned. The sample with the MeO4+Me4 demonstrates the fastest carrier extraction (i.e., smallest τ_{ave}) compared to the MeO4+Me2 and Me2+2PACz. To gain more insight into the free carrier dynamics in $MAPbI_3$ and the hole collection by mixed-SAMs layers, we carried out time-resolved microwave conductivity (TRMC) measurements (see Figure S4−S6). The resulting half-lifetime ($\tau_{1/2}$) extracted from the spectra, as shown in Figure S6, is plotted as a function of the number of excitations in Figure 1f. The MeO4+Me4 and MeO4+Me2 samples showed extended carrier lifetime compared to Me2+2PACz and reference (w/o SAMs) samples, demonstrating effective hole extraction so that electrons left in the $MAPbI_3$ layer existed for a longer time (Figure S6).[31,32] Hence, TRMC results corroborate the PL outcomes.[33] Based on the observation above, we can preliminarily conclude that the most promising mixed-SAMs combination is MeO4+Me4 linked to enhanced device performance by improving the quality of mixed-SAMs/PVK interfacial contact.

To further elucidate the processes occurring during codeposition and determine the reason why a specific mixed-SAMs combination functions effectively as an HTL while others do not, we conducted a series of X-ray photoelectron spectroscopy (XPS) analyses on the mixed-SAMs codeposited samples. To enable these measurements, a controlled washing procedure (Step 1), shown in Figure 2a, was carried out on the sample by applying different doses of DMF solvent ranging from 5 to 100 μL to progressively remove the $MAPbI_3$ film and ultimately expose the underlying MeO4+Me4 interface. After each dose of the washing procedure, we conducted surface XPS scans of the interface of the $MAPbI_3$/MeO4+Me4/ITO sample (Figure S7a). The XPS results indicate that with increasing DMF solvent dose, more $MAPbI_3$ components are removed, as evidenced by the decreasing intensity of the Pb 4f peak at 138.98 eV (Figure S7b). When the DMF solvent dose reaches 100 μL, the Pb 4f peak intensity at the measurement location diminishes to a level that is comparable to that of the P 2p peak (Figure S7b). This observation confirms the presence of phosphorus signals originating from the mixed-SAMs molecules, demonstrating that the codeposition process is an effective method for simultaneously forming the perovskite layer and the mixed-SAMs-based HTL layer at the bottom of the sample. The atomic ratios of Pb and P as a function of the DMF dose are shown in Figure S7c. The full set of measured elements is found in Figure S7d and Tables S4−S5. To assess the different coverage rates of various mixed-SAMs combinations on the ITO surface, we performed a similar procedure (Figure 2a) on all mixed-SAMs samples, washing them directly with 100 μL of DMF solvent to remove the $MAPbI_3$ layer from the surface (Figure 2a step 1). XPS surface scanning measurements are presented in Figure S8a,d, showing the interaction between the anchoring groups of SAMs molecules and the ITO substrate. The O 1s spectrum of ITO exhibits four deconvoluted peaks at a binding energy of 530, 531, 532, and 533 eV, corresponding to In/Sn−O, surface oxygen vacancies (V_o), In−O−H, and H_2O, respectively.[34] For the O 1s spectra of mixed-SAMs/ITO samples, the fitted peaks correspond to In/Sn−O, surface oxygen vacancies (V_o), and In−O−H/In−O−P. Compared to the ITO reference sample shown in Figure S8d, the O 1s peak area ratio of $area_{In-O-P/In-O-H}$ to $area_{In/Sn-O}$ gradually increases for the different mixed-SAMs combinations. This observation can be linked to an increased relative surface coverage factor.[35] We found that for the three mixed-SAMs combinations, Me2+2PACz, MeO4+Me2, and MeO4+Me4, the coverage factor is 30.56, 66.24, and 80.13%, respectively, as shown in Figure 2b (additional details are reported in Table S6). This trend suggests that the MeO4+Me4 mixed-SAMs combination effectively enhances ITO substrate coverage, which is essential for achieving superior device performance.[34,35] Since XPS is a point measurement technique, the large area uniformity of the mixed-SAMs needs to be further investigated.

To investigate the failure mechanism of the Me2+2PACz sample working as the HTL discussed in TRMC and PL tests, we performed XPS surface scanning and depth etching analysis. We hypothesize that during the co-deposition process, the Me2+2PACz are not fully extruded downward to the bottom interface during the $MAPbI_3$ crystallization.[17,19] Consequently, the Me2+2PACz layer failed to function as an effective HTL; instead, the Me2+2PACz molecules are distributed within the $MAPbI_3$ film. Yet the XPS element depth analysis does not show any direct information about the P 2p signal, as shown in Figure S9 and Tables S7−S9. We then analyzed the possible reasons for this unexpected result. Given

https://doi.org/10.1021/acsami.5c18266
ACS Appl. Mater. Interfaces 2025, 17, 67306−67317

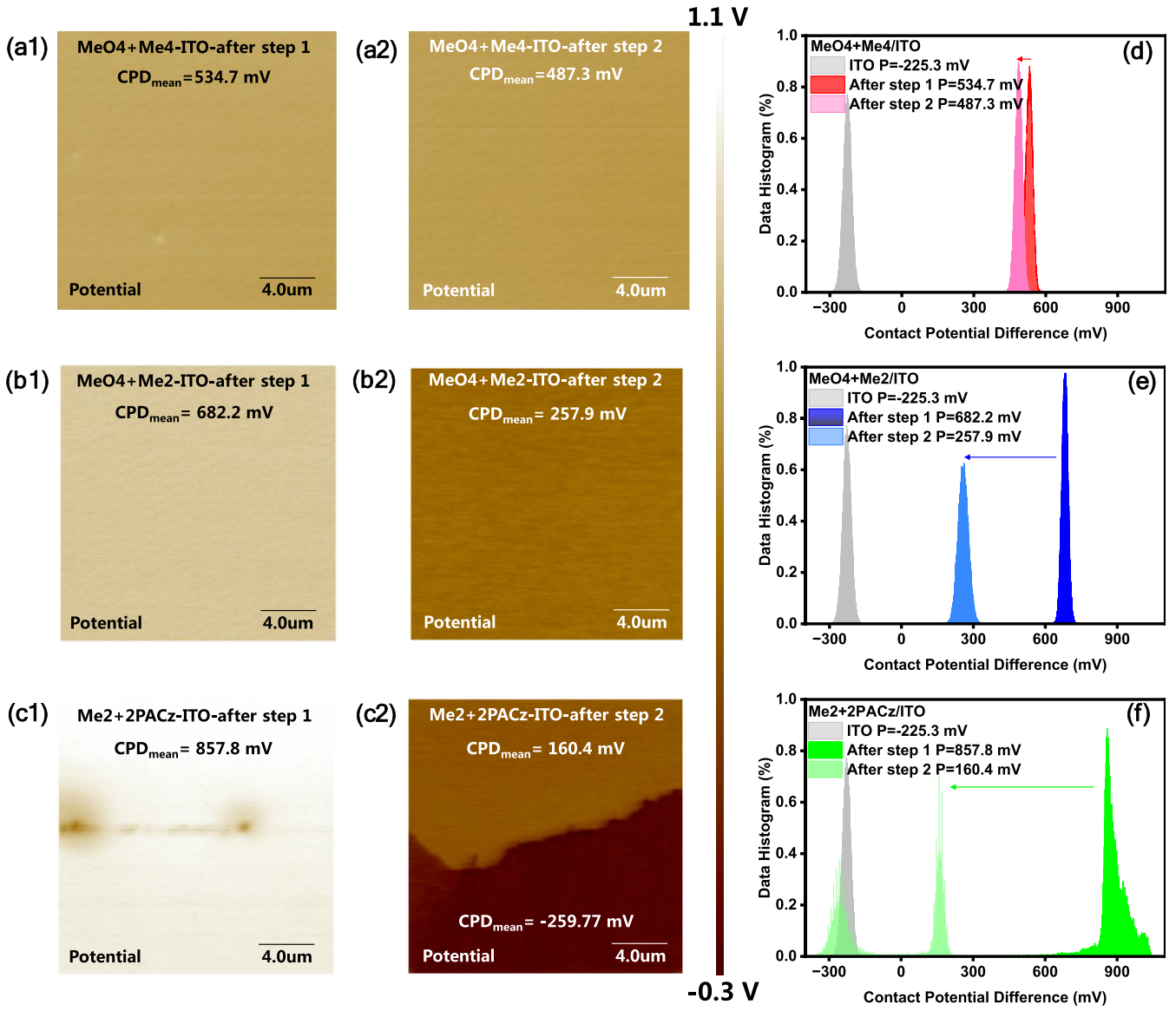

Figure 3. KPFM results of bonding strength between different mixed-SAMs and the ITO substrate. Contact potential difference (CPD) distribution and mean value after DMF wash step 1 and step 2 (see Figure 2a) of (a1-a2) MeO4+Me-4/ITO, (b1-b2) MeO4+Me2/ITO, and (c1-c2) Me2+2PACz/ITO samples. (d–f) Statistical distribution of mean CPD value difference before and after DMF wash of different mixed-SAMs/ITO samples elaborated from the images in panels (a–c). The KPFM-based ITO distribution is added as a reference in Figure S19.

that the mixed-SAMs concentration in the 2.5 × 2.5 cm sample is extremely low, we estimated that the net mixed-SAMs content per sample is approximately 2 μg, with the corresponding phosphorus content regarding atom numbers in each molecule being only 1/33 for 2PACz and 1/47 for MeO-4PACz, as shown in Figure S20. If the Me2+2PACz did not accumulate at the bottom interface and bind to the ITO substrate but were instead dispersed throughout other regions, the elemental concentration of phosphorus atoms would be further diluted and might have fallen below the detection limit of the XPS instrument.[36] XPS surface scanning measurements were performed from both sides of the samples and for all three $MAPbI_3$/mixed-SAMs combinations, as shown in Figures 2c and S10a. The solid line plots clearly demonstrate the Pb 4f and I 3d peak shifts toward the lower binding energy direction, which can be attributed to the increased electron density caused by MeO and P═O from SAMs binding with uncoordinated Pb and I atoms at the bottom surface.[4,30,37,38]

As shown in Table S10, the greater the degree of peak shifts, the more functional groups are bonded: MeO4+Me4 > MeO4+Me2 > Me2+2PACz. While at the top surface, only the MeO4+Me4 sample demonstrates the same shift direction (dashed lines in Figures 2c, S10a, and Table S11).

The MeO4+Me2 and Me2+2PACz samples demonstrate opposite peak shift direction at the top surface of $MAPbI_3$ toward the higher binding energy direction (Table S11), which can be attributed to less MeO and P═O being bonded.[38] However, it is reported that after the co-deposition process, SAMs signals can be observed at both the top and bottom surfaces of the PVK layer via the time-of-flight secondary ion mass spectrometry (TOF-SIMS) test.[17,19] Here, we only observed MeO4+Me4 with an obvious signal at the top surface of the $MAPbI_3$ layer, which means that the extrusion effect of MeO4+Me4 in the $MAPbI_3$ precursor is the best (solid line plots in Figure 2c, Table S10). In addition, we also found that the I 3d and Pb 4f peaks of the $MAPbI_3$/

https://doi.org/10.1021/acsami.5c18266
ACS Appl. Mater. Interfaces 2025, 17, 67306–67317

MeO4+Me4 sample after 5, 60, and 100 μL DMF wash showed varying degrees of shift toward higher binding energy direction (Figure S10b,c, and Table S12). This indicates that the DMF can effectively dissociate the binding between MeO/P═O and I/Pb, which also implies that the solvation interaction between SAMs and solvents (DMF:DMSO) is much stronger than the interaction between SAMs and PVK components.[18,38] To get a more comprehensive landscape of the SAMs-PVK co-deposition process, the solvation interaction between SAMs and solvents has to be taken into consideration. The valence band spectra of $MAPbI_3$/mixed-SAMs samples were also gained from XPS surface scanning as shown in the Figure S11. No obvious valence band energy change of any SAMs-doped/modified $MAPbI_3$ samples can be observed, which suggests that the trace amount of SAMs within the $MAPbI_3$ film does not affect the film's properties, as reconfirmed by the absorption and XRD results (Figures S5 and S12).

Based on the coverage difference of different mixed-SAMs combinations, we further conducted morphological characterization of $MAPbI_3$ films co-deposited with different mixed-SAMs. The average grain size elaborated from scanning electron microscopy (SEM) top-view images of the PVK surface is reported in Figures S13−S14. The reference $MAPbI_3$ sample w/o HTL has the lowest average grain size of 247.85 nm ($MAPbI_3$/ITO), while the three different co-deposited mixed-SAMs result in an increased value in the range between 329 and 370 nm (MeO4+Me2 < MeO4+Me4 < Me2+2-PACz). This indicates that the mixed-SAMs favor larger grain size formation of $MAPbI_3$. The largest grain size obtained for $MAPbI_3$/Me2+2PACz/ITO could be attributed to its passivation effect (Figure 1d), which can also be corroborated by the XRD results in Figure S12.[30,39,40] Since the SEM results did not provide conclusive insights of $MAPbI_3$ film quality, we further performed AFM surface morphology measurements on $MAPbI_3$ films deposited on different mixed-SAMs layers to assess the film uniformity. To ensure the generality of our conclusions, we selected two scanning sizes: 2 × 2 and 20 × 20 μm^2. From the AFM images reported in Figures S15−S16, the surface roughness (R_a) was detected as shown in Figures 2d and S17. By comparing R_a values, we obtained the roughness variation trend, with specific values shown in Table S13. For the 4 μm^2 scan size, all three mixed-SAMs combinations resulted in a lower surface roughness of $MAPbI_3$ films compared with their calculated average values. For the 400 μm^2 scan size, the MeO4+Me4 sample exhibited the greatest reduction in roughness, while the Me2+2PACz sample showed an increase in roughness compared to the calculated average. Across both scan sizes, the MeO4+Me4 sample consistently achieved the greatest reduction in $MAPbI_3$ layer roughness (R_a), highlighting its superior performance (Figure S18).

Furthermore, we performed KPFM measurements of the mixed-SAM layer at the buried interface of the $MAPbI_3$ films to evaluate its binding strength with the ITO substrate. First, we washed the samples with 100 μL of DMF to remove the $MAPbI_3$ layer and expose the buried mixed-SAMs layer (Figure 2a, step 1). We then conducted KPFM scanning with a 20 × 20 μm^2 scan size to obtain the contact potential difference (CPD) distribution. Figure 2e and Table S14 show the calculated WF: MeO4+Me4 ≈ −5.37 eV (red), MeO4+Me2 ≈ −5.55 eV (blue), and Me2+2PACz ≈ −5.55 eV (green).[15,41] For completeness, we report the WF of Au (−5.1 eV) and ITO (−4.7 eV) and the WF values calculated for tip calibration reference before each measurement.[41−45] Based on the WF results, among all three mixed-SAMs combinations, the MeO4+Me4 is the most suitable HTL for $MAPbI_3$ (HOMO = −5.4 eV).[4,27] Subsequently, we performed an additional 100 μL of DMF wash to remove weakly bonded SAMs molecules from the ITO surface (step 2 in Figure 2a), followed by another KPFM scan to obtain the CPD distribution after the second washing step. Figure S19 presents the CPD distribution of fresh ITO as a reference sample. The CPD differences before and after DMF washing (step 2 Figure 2a) are compared in Figure 3a−c, with the following trend (from smallest to largest difference): MeO4+Me4/ITO < MeO4+Me2/ITO < Me2+2PACz/ITO (Figure 3d−f).[45] The CPD difference for the MeO4+Me4 sample is limited to only ∼50 mV (Figure 3d), demonstrating its exceptional binding strength with ITO. In contrast, the CPD difference for MeO4+Me2 goes up to ∼ 420 mV (Figure 3e), while for Me2+2PACz (Figure 3f), we detected the highest variation of ∼700 mV. It is worth noting that the latter mixed-SAMs have very low homogeneity, with half of the scanned area showing complete exposure of the ITO surface (Figures 3c2, S19), indicating the weakest binding strength.[35]

One of the primary design considerations for SAMs materials is the ensuring molecular rigidity. This is to maintain strong interfacial bonding, thereby providing excellent optical, electrical, and mechanical properties to enhance device stability and prevent interface defects that could lead to performance degradation. In SAMs molecules, the rigidity of the carbazole headgroup is intrinsically ensured by its molecular structure. However, during the self-assembly process on the ITO surface, the $-PO_3H_2$ anchor group retains a high degree of conformational flexibility. If it fails to form strong binding interactions with ITO, several interface defects could arise during long-term operation.[10] It is worth noting that, according to previous literature, the interfacial binding strength and performance of Me-2PACz and 2PACz are not significantly inferior to other SAMs materials.[46−48] The unexpectedly weak binding observed in our study is likely attributed to the co-deposition processing method we used, corresponding to the discussion above of Figure S10b,c, which has unique dynamics and will be thoroughly discussed in the quantum chemistry calculations section. In summary, the DMF washing test of mixed-SAMs materials indicates that MeO4+Me4 exhibits the best compatibility with the co-deposition process and interfacial binding strength with ITO.

To further understand the selectivity of the codeposition process for mixed-SAMs and elucidate the interaction between SAMs and the DMF:DMSO solvent system, it is first necessary to thoroughly investigate the crystallization process of PVK solution films under hot-plate annealing conditions. According to the study by Huang et al., for the $MAPbI_3$ thin film prepared by spin-coating in a DMF/DMSO system, it is widely accepted that the crystallization progresses in a top-down direction following two phases.[26] The hot plate heats the sample from the bottom (substrate side), inducing convective flows of the solvent within the liquid film along the vertical direction. The solvent (coordinating DMSO) initially evaporates from the upper surface of the liquid film, initiating crystallization at the top surface. In the early 0−1s, the semitransparent wet film rapidly turns black. From 1 to 3s, the film begins to crystallize from top to bottom, with perovskite grains first appearing in the upper half of the film.[26] The intermediate phase (MAI-PbI_2-DMSO) remains in the lower half of the film, with the

https://doi.org/10.1021/acsami.5c18266
ACS Appl. Mater. Interfaces 2025, 17, 67306−67317

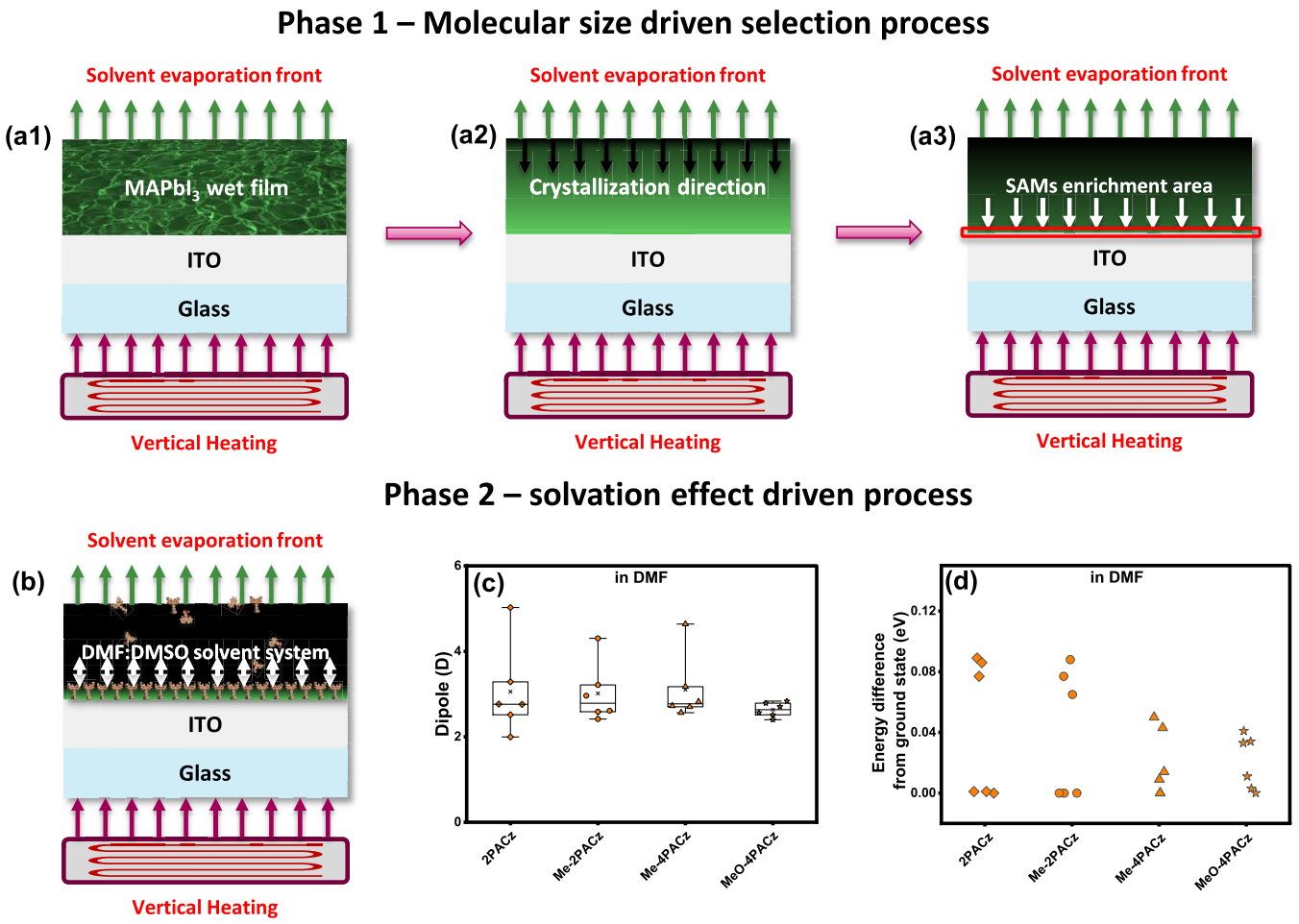

Figure 4. Molecular size and solvation effect-driven selection process of co-deposition. (a) Demonstration of phase 1 in co-deposition. (b) Demonstration of phase 2 in co-deposition. (c, d) Calculated total energies with respect to the lowest energy conformer (indicated as 0 eV) of the SAMs molecules and their electrostatic dipole moments in DMF.

proportion of the intermediate phase gradually decreasing and its spatial distribution decreasing closer to the bottom interface.[49,50] In the first annealing phase (0−3 s), almost all of the intermediate phase transforms into the perovskite phase, terminating at the bottom surface. During the second annealing phase (3 s−60 s−10 min), the transformation rate of the remaining intermediate phase significantly slows down until it completely disappears. This is because the top surface of the PVK-$MAPbI_3$ film has already been solidified, and the residual DMSO requires more time to evaporate.

Based on the crystallization process summarized above, several phenomena occur: solvent−solute interactions, crystallization kinetics, and size exclusion effects. The entire crystallization process can be divided into two distinct phases summarized in Figure 4: the size-driven selection process and the solvation effect-driven process. In phase 1 (Figure 4a1-a3), since $MAPbI_3$ is present as a saturated solution (1.4 M), while the concentration of mixed-SAMs (0.25 mg/mL) is significantly below its solubility limit (>10 mg/mL), $MAPbI_3$ preferentially undergoes nucleation and crystallization from top to down. As the crystal growth front advances downward, the significantly larger molecular size of SAMs (≈9−13 Å) compared with the $MAPbI_3$ unit cell (≈6.3 Å) prevents their incorporation into the $MAPbI_3$ lattice (Table S15). Additionally, due to their low concentration and relatively weaker solvation interaction with solvents compared to $MAPbI_3$, SAMs molecules are displaced into the remaining liquid phase rather than precipitated and solidified, which reside in the lower solution layer. During the exclusion process in phase 1, the molecular size of SAMs is a decisive factor: larger molecules experience stronger exclusion along the $MAPbI_3$ crystallization direction, while smaller molecules have a higher probability of remaining within the perovskite grain boundaries or other defect regions, as shown in Figure S20.[26,51−53] As $MAPbI_3$ crystallization nears completion, SAMs molecules may accumulate at the bottom surface of the residual liquid region. Ultimately, when the solvent evaporates to a critical level (probably after 3s of annealing), SAMs begin to precipitate and deposit onto the ITO substrate (enrichment area).

It is worth mentioning that the co-deposition method not only simplifies the fabrication process but also accelerates the self-assembly process of SAMs molecules on the ITO surface. In conventional spin-coating techniques for SAMs layer preparation, SAMs solutions are typically deposited onto the ITO surface and left undisturbed for up to tens of minutes before spin-coating the PVK solution on top, allowing sufficient time for self-assembly.[5] We propose that solvation effects are a key factor influencing the final film quality of different mixed-SAMs combinations on the ITO substrate, as shown in Figure 4b. The stronger the solute−solvent interactions, the slower the solute precipitation rate during the crystallization process of a supersaturated solution.[54]

https://doi.org/10.1021/acsami.5c18266
ACS Appl. Mater. Interfaces 2025, 17, 67306−67317

Combined with rapid solvent evaporation during annealing, the available time for mixed-SAMs to precipitate and self-assemble on the ITO surface is reduced, which may ultimately affect film formation. Therefore, in phase 2 (Figure 4b), where SAMs molecules bind to the ITO surface, the strength of the interaction between SAMs and the DMF:DMSO solvent system is the decisive factor. Considering that SAMs molecules possess aromatic ring structures and permanent dipole moments, their solubility characteristics in the DMF:DMSO mixed solvent system are influenced by $\pi-\pi$ interactions, hydrogen bonding, intermolecular van der Waals forces, and polarity effects. According to the Hansen solubility parameters (HSP) theory, solubility contributions can be divided into three primary components: dispersion forces (D_f), polarity forces (P_f), and hydrogen bonding interactions (H_f), as described by eq 1:[55]

$$\delta_T^2 = \delta_D^2 + \delta_P^2 + \delta_H^2 \quad (1)$$

where δ_T represents the total solubility parameter (Total Hansen Solubility Parameter). δ_D, δ_P, and δ_H correspond to the dispersion force, polarity force, and hydrogen bonding force parameters, respectively (unit: $MPa^{1/2}$). Among these, $\pi-\pi$ interactions are classified as dispersion forces. DMF exhibits relatively weak $\pi-\pi$ interactions; however, its C═O functional group can act as a π-electron acceptor, engaging in weak $\pi-\pi$ interactions with aromatic rings (Figure S21−22). DMSO primarily relies on hydrogen bonding and dipole−dipole interactions, contributing minimally to $\pi-\pi$ interactions. Moreover, given the low concentration of SAMs molecules in the solution, solute−solute $\pi-\pi$ stacking interactions can be considered negligible.[55] For hydrogen bonding interactions, both DMF and DMSO exhibit strong hydrogen bond acceptor capabilities.[56−60] Given the structural, size, and functional group similarities among the four SAMs molecules we used and the primary hydrogen bonding interactions in this system occurring between the solvent molecules and the $-PO_3H_2$ anchor group, the contribution of hydrogen bonding among different SAMs molecules in terms of solvation effects is similar.[61−65] As a result, the contributions of δ_D and δ_H can be approximated as a constant C, leading to a simplified form of the HSP equation in this system.

$$\delta_T^2 \propto \delta_P^2 + C \quad (2)$$

We further analyzed the influence of different SAMs' polarity parameters on their solvation behavior. Within SAMs molecules, both the carbazole headgroup and the $-PO_3H_2$ anchor group possess permanent dipole moments. However, the dipole moment contribution from the carbazole moiety is relatively small. In contrast, within the $-PO_3H_2$ group, the asymmetric electron cloud distribution of the P═O and P−OH bonds results in a nonzero net dipole moment, conferring a substantial permanent dipole moment (Figure S21).[66] Although all SAMs molecules share the same anchor group, variations in the carbon chain length alter the overall dipole moment contribution of the anchor group to the molecule. To quantify these effects, we performed quantum chemistry simulations to compute the orientation-dependent dipole moments of the four SAMs molecules in vacuo, DMF, and DMSO environments, as shown in Figures 4c,d, S23, and Table S16−S18. Although the carbazole headgroup is considered rigid, the carbon chain tail possesses a degree of rotational freedom in solution, enabling self-assembly onto the ITO surface. Our quantum chemistry calculations on six different conformers of 2PACz, Me-2PACz, Me-4PACz, and MeO-4PACz reveal that MeO-4PACz has, on average, a dipole moment lower than those of the other molecules. Additionally, the potential energy landscape of MeO-4PACz appears to be much flatter compared to that of the other molecules. For 2PACz, Me-2PACz, and Me-4PACz, certain conformers exhibit rather large dipole moments, contrary to MeO-4PACz, where differences in dipole moments among various conformers are less pronounced. As a consequence, given the available energy in the environment, higher dipole states of 2PACz, Me-2PACz, and Me-4PACz can be observed, leading to stronger interactions with solvents, supporting our earlier discussion. As shown in Figures 4c,d and S22, we listed the dipole moment difference (D) of different SAMs molecules under the same energy level and solvent environment. The dipole moment distribution follows the order: $D_{2PACz} \geq D_{Me\text{-}2PACz} \approx D_{Me\text{-}4PACz} \geq D_{MeO\text{-}4PACz}$. Hence, we have

$$\delta^2_{T_{MeO-4PACz}} \leq \delta^2_{T_{Me-4PACz}} \approx \delta^2_{T_{Me-2PACz}} \leq \delta^2_{T_{2PACz}} \quad (3)$$

Thus, we could preliminarily conclude that the MeO4+Me4 mixed-SAMs combination exhibits the weakest interaction with the DMF:DMSO mixed solvent system, whereas Me2+2PACz exhibits the strongest interaction. Considering both the molecular size of SAMs and their solvation effects, we can explain why the MeO4+Me4 mixed-SAMs combination achieves better coverage on the ITO surface. During phase 1, this combination is effectively excluded from the lower region beneath the PVK layer, and in phase 2, it can more readily detach from the DMF:DMSO solvent system. In contrast, the Me2+2PACz mixed-SAMs combination, due to its smaller molecular size and stronger interaction with the DMF:DMSO mixed solvent system, experiences greater difficulty in detaching from the DMF:DMSO solvent system (desolvation), thereby hindering its ability to form hydrogen bonds and self-assemble on the ITO surface. Consequently, during the $MAPbI_3$ crystallization process, these SAMs molecules may become trapped at grain boundaries or other regions. If $MAPbI_3$ crystals continue to grow, Me-2PACz and 2PACz may function as surface modification molecules, contributing to defect passivation.[40]

CONCLUSIONS

In summary, this study investigates the co-deposition process of mixed-SAMs of four commercial SAMs materials (MeO-4PACz, Me-4PACz, Me-2PACz, and 2PACz) with $MAPbI_3$ precursor solutions and compares their performance with that of single SAMs. The results demonstrate that in the device architecture ITO/Mixed-SAMs/$MAPbI_3$/PCBM/BCP/Ag, using mixed-SAMs as the HTL outperforms the single SAM in photovoltaic performance. Among the three tested combinations, MeO-4PACz + Me-4PACz was identified as the optimal pairing, yielding the best device performance and reproducibility. Additionally, we quantitatively studied the interfacial properties and energy-level modulation differences among various mixed-SAMs combinations. The results revealed that the MeO-4PACz + Me-4PACz combination achieved the best substrate coverage (80.13%) and interfacial contact during the co-deposition process. Its mechanical bonding strength with the ITO substrate was the strongest, providing a foundation for stable device operation. Furthermore, KPFM measurements revealed that this combination

https://doi.org/10.1021/acsami.5c18266
ACS Appl. Mater. Interfaces 2025, 17, 67306−67317

exhibited the most favorable energy-level alignment with a WF of −5.37 eV. To further elucidate the mechanism of mixed-SAMs + PVK co-deposition, we conducted quantum chemistry calculations on the SAMs molecules in vacuo, DMF, and DMSO environments. We observed that MeO-4PACz has, on average, a lower dipole moment than the other SAMs molecules studied in this manuscript and hence potentially less interaction with the DMF:DMSO solvent. These results were analyzed in conjunction with the spin-coating−annealing−crystallization process. We propose that the mixed-SAMs + PVK co-deposition process is driven by two factors: the molecular size and the dipole moment of the SAMs. Larger SAMs molecules are more likely to be extruded to the bottom interface during the annealing and crystallization of the perovskite precursor, forming a compact HTL. Additionally, SAMs with smaller dipole moments exhibit weaker interactions with the polar solvent, allowing faster separation from the solvent during annealing, which facilitates layering with the perovskite rather than remaining embedded within the PVK layer. Our findings provide new perspectives and explanations for the use of SAMs materials in PSC fabrication and offer guidance for their processing simplification.

EXPERIMENTAL METHODS

Materials Purchase and Film Preparation. CH_3NH_3I (MAI) (99.9%), PbI_2 (99.999%), $PC_{61}BM$, and BCP were purchased from Advanced Election Technology Co., Ltd. MeO-4PACz, Me-4PACz, Me-2PACz, and 2PACz were purchased from TCI Chemicals. DMF, DMSO, CB, DCB, and IPA solvents were purchased from Sigma-Aldrich. Ag slugs were purchased from Sigma-Aldrich. ITO substrates were purchased from Advanced Election Technology Co., Ltd. PTFE filters were purchased from TCI Chemicals. All materials were used as received.

Precursor Preparation. MAI and PbI_2 with a 1:1 ratio were added into a DMF:DMSO (9:1) mixed solvent to prepare the 1.4 M $MAPbI_3$ solution. MeO-4PACz, Me-4PACz, Me-2PACz, and 2PACz were added into DMF solvent to prepare a 10 mg/mL single SAM solution. The single SAM solution was added to the prepared $MAPbI_3$ solution to prepare a single (0.25 mg/mL) or mixed-SAMs (0.25 mg/mL)/$MAPbI_3$ mixed solution. Molar ratio of mixed-SAMs is 1:1. $PC_{61}BM$ was added into DCB solvent to prepare a $PC_{61}BM$ solution (20 mg/mL). BCP was added to the IPA solvent to prepare the BCP solution (0.5 mg/mL). All solutions were stirred by a vortex mixer for 2h. $MAPbI_3$ precursors and $PC_{61}BM$ solution were filtered by a PTFE filter (Φ = 0.25 μm) before use.

Device Fabrication. ITO substrates were sonicated in DI water (with detergent) and ethanol for 10 min, and the process was repeated 3 times. After a 20 min UVO-plasma treatment, ITO substrates were ready to use. For reference samples, Me-4PACz +$MAPbI_3$ mixed solution was spin-coated onto ITO substrates (4000 rpm for 30 s) to prepare the hole transporting layer and perovskite layer at the same time. 200 mL of CB solvent was used as an antisolvent and dropped at 25 s before the spin-coating finished. For mixed-SAM codeposition samples: Mixed-SAMs+$MAPbI_3$ mixed solution was spin-coated onto ITO substrates (4000 rpm for 30 s) to prepare the hole transporting layer and perovskite layer at the same time. 200 mL of CB solvent was used as antisolvent and dropped at 25 s before the spin-coating finished. For all solar cell devices, $PC_{61}BM$ solution was spin-coated onto perovskite layer as electron transporting layer (2000 rpm for 30 s). Then BCP solution was spin-coated onto the PCBM layer as buffer layer. In the end, a 100 nm Ag layer was deposited by thermal evaporation as a metallic electrode.

Sample Preparation for XPS and KPFM. For DMF washing, 5−100 μL of DMF solvent were dropped onto $MAPbI_3$/Mixed-SAMs/ITO samples and then spun (5000 rpm for 30 s).

Characterization. X-ray diffraction (XRD) patterns were measured with a Bruker D8 Advance diffractometer equipped with a Cu Kα X-ray source that has a wavelength of 1.54 Å. The elemental composition of the PVK films was tested by X-ray photoelectron spectroscopy (XPS) with a ThermoScientific K-α spectrometer. The spectrometer is equipped with a focused monochromatic Al−Kα X-ray source (1486.6 eV) operating at 36 W (12 kV, 3 mA). The spot size is approximately 800 × 400 μm^2. The pass energy of the analyzer was set to 50 eV. A flood gun was operated at 1 V and 100 μA to prevent charging of the sample. The base pressure in the analysis chamber was approximately 2 × 10^{-9} mbar. Three points are tested for each sample to take an average. Depth profiling was performed by etching the sample with argon ions. The voltage of the ion gun was set to 1000 eV for in-depth etching of all samples. Detailed analysis was performed with Avantage software, where 70% Gaussian and 30% Lorentzian line shapes (weighted least-squares fitting method) and a nonlinear Shirley-type background were used to fit the peaks. Atomic percentages were calculated based on the fitted peak areas and the corresponding sensitivity factors of the detailed scans. The binding energy was corrected for the charge shift by taking the done relative to the primary C 1s hydrocarbon peak at BE = 284.8 eV as a reference. The surface morphology of the PVK films was tested by the scanning electron microscope (SEM, JEOL) with an accelerating voltage of 5 keV. The atomic force microscopy (AFM) and the Kelvin probe force microscopy (KPFM) scans of PVK and SAMs films were carried out with a Bruker Dimension Icon AFM system with an SCM-PIC-V2 probe in ambient air. The PFKPFM-SMPL reference sample by Bruker was used to calibrate the work function (WF) of the probes. The absorptance spectra were tested by ultraviolet−visible spectroscopy (UV/vis, PerkinElmer, Lambda 1050) within a wavelength range of 300−800 nm. The photoluminescence (PL) spectra of the samples were investigated by the steady-state photoluminescence (SSPL, FLS 980) setup with an excitation wavelength of 420 nm. The emission light was filtered with a 550 nm filter. The time-resolved photoluminescence (TRPL) was measured with a Lifespec setup with an excitation wavelength of 405 nm. The detailed measurement was described in the corresponding reference.[67] Time-resolved microwave conductance (TRMC) was applied to learn about the carrier lifetime, mobility, and trap densities. All of the measurement parameters are found in the corresponding reference.[31]

Computational Details. All quantum chemistry calculations were performed using the Amsterdam Modeling Suite (AMS).[68] Geometry optimizations for six different conformers of 2PACz, Me-2PACz, Me-4PACz, and MeO-4PACz were carried out using density functional theory (DFT) with the B3LYP functional and the TZ2P basis set. To account for solvent effects, we employed the COnductor-like Screening MOdel (COSMO) as implemented within AMS.[69] The COSMO model treats the solvent as a polarizable continuum, allowing for efficient calculation of the solvation effects on molecular properties. Conformational analysis was conducted by rotating relevant dihedral angles in 120° increments, followed by full geometry optimizations of the resulting structures. Ultimately, six conformers for each molecule were selected for further analysis. Dipole moments were computed for each optimized conformer using the same level of theory as for the geometry optimizations. All molecular visualizations were created by using the integrated graphical user interface provided by the AMS.

ASSOCIATED CONTENT

Supporting Information

The Supporting Information is available free of charge at https://pubs.acs.org/doi/10.1021/acsami.5c18266.

Supporting discussions, additional figures. Including solar cell structure and performance, TRPL, absorptance, and TRMC results and discussions, XPS surface scan and depth profiling results, XRD and SEM results, AFM topography and KPFM surface potential results, SAM molecule configurations, molecule sizes, molecule coulomb potential distributions, molecule dipoles, and total energies by quantum chemistry calculations (PDF)

https://doi.org/10.1021/acsami.5c18266
ACS Appl. Mater. Interfaces 2025, 17, 67306−67317

AUTHOR INFORMATION

Corresponding Authors

Haoxu Wang − *PVMD Group, Delft University of Technology, 2628 CD Delft, The Netherlands;* orcid.org/0000-0002-5430-0899; Email: h.wang-18@tudelft.nl

Luana Mazzarella − *PVMD Group, Delft University of Technology, 2628 CD Delft, The Netherlands;* Email: l.mazzarella@tudelft.nl

Authors

Jin Yan − *PVMD Group, Delft University of Technology, 2628 CD Delft, The Netherlands*

Mare Dijkstra − *PVMD Group, Delft University of Technology, 2628 CD Delft, The Netherlands*

Engin Torun − *PVMD Group, Delft University of Technology, 2628 CD Delft, The Netherlands*

Moumita Rana − *PVMD Group, Delft University of Technology, 2628 CD Delft, The Netherlands;* orcid.org/0000-0002-9348-4491

Paul Procel Moya − *PVMD Group, Delft University of Technology, 2628 CD Delft, The Netherlands;* orcid.org/0000-0003-4997-3551

Rudi Santbergen − *PVMD Group, Delft University of Technology, 2628 CD Delft, The Netherlands*

Miro Zeman − *PVMD Group, Delft University of Technology, 2628 CD Delft, The Netherlands*

Olindo Isabella − *PVMD Group, Delft University of Technology, 2628 CD Delft, The Netherlands*

Complete contact information is available at: https://pubs.acs.org/10.1021/acsami.5c18266

Author Contributions

H.W. conceived the project and performed the experiments, data analysis, and experimental planning. The project was supervised by Prof. O.I. and Dr. L.M. The quantum chemistry calculations were performed by Dr. E.T. The XPS test was performed by Dr. J.Y. The TRMC test was performed by M.D. The manuscript was written by H.W. All the authors reviewed the manuscript.

Notes

The authors declare no competing financial interest.

ACKNOWLEDGMENTS

H.W. acknowledges the China Scholarship Council (CSC No. 202108610082) for financial support. In addition, the authors thank Dr. Tom Savenije for facilitating interactions with the OM group, TU Delft. The authors also thank Martijn Tijssen, Bernardus Zijlstra, and Stefaan Heirman from the PVMD group, TU Delft, and Marcel Bus, Xiaohui Liu, Jos Themie, and Duco Bosma from the OM group, TU Delft, for their technical support.

REFERENCES

(1) NREL. *Best Research-Cell Efficiency Chart. Photovoltaic Research*, https://www.nrel.gov/pv/cell-efficiency (accessed July 11, 2025).

(2) Jia, L.; Xia, S.; Li, J.; Qin, Y.; Pei, B.; Ding, L.; Yin, J.; Du, T.; Fang, Z.; Yin, Y.; Liu, J.; Yang, Y.; Zhang, F.; Wu, X.; Li, Q.; Zhao, S.; Zhang, H.; Li, Q.; Jia, Q.; Liu, C.; Gu, X.; Liu, B.; Dong, X.; Liu, J.; Liu, T.; Gao, Y.; Yang, M.; Yin, S.; Ru, X.; Chen, H.; Yang, B.; Zheng, Z.; Zhou, W.; Dou, M.; Wang, S.; Gao, S.; Chen, L.; Qu, M.; Lu, J.; Fang, L.; Wang, Y.; Deng, H.; Yu, J.; Zhang, X.; Li, M.; Lang, X.; Xiao, C.; Hu, Q.; Xue, C.; Ning, L.; He, Y.; Li, Z.; Xu, X.; He, B. Efficient Perovskite/Silicon Tandem with Asymmetric Self-Assembly Molecule. *Nature* **2025**, *644*, 1−3.

(3) Dahal, B.; Li, W. Configuration of Methylammonium Lead Iodide Perovskite Solar Cell and Its Effect on the Device's Performance: A Review. *Adv. Mater. Interfaces* **2022**, *9* (19), No. 2200042.

(4) Chang, X.; Yang, G.; Tan, Y.; Peng, Y.; Wu, W.-Q. Self-Assembled Molecule-Assisted Simplified Processing of High-Performance Solar Cells and Light-Emitting Diodes. *Sol. RRL* **2024**, *8* (11), No. 2400182.

(5) Cheng, H.; Li, Y.; Zhong, Y. Towards Cost-Efficient and Stable Perovskite Solar Cells and Modules: Utilization of Self-Assembled Monolayers. *Mater. Chem. Front.* **2023**, *7* (18), 3958−3985.

(6) Wang, J.; Jiao, B.; Tian, R.; Sun, K.; Meng, Y.; Bai, Y.; Lu, X.; Han, B.; Yang, M.; Wang, Y.; Zhou, S.; Pan, H.; Song, Z.; Xiao, C.; Liu, C.; Ge, Z. Less-Acidic Boric Acid-Functionalized Self-Assembled Monolayer for Mitigating NiOx Corrosion for Efficient All-Perovskite Tandem Solar Cells. *Nat. Commun.* **2025**, *16* (1), No. 4148.

(7) Al-Ashouri, A.; Magomedov, A.; Roß, M.; Jošt, M.; Talaikis, M.; Chistiakova, G.; Bertram, T.; Márquez, J. A.; Köhnen, E.; Kasparavičius, E.; Levcenco, S.; Gil-Escrig, L.; Hages, C. J.; Schlatmann, R.; Rech, B.; Malinauskas, T.; Unold, T.; Kaufmann, C. A.; Korte, L.; Niaura, G.; Getautis, V.; Albrecht, S. Conformal Monolayer Contacts with Lossless Interfaces for Perovskite Single Junction and Monolithic Tandem Solar Cells. *Energy Environ. Sci.* **2019**, *12* (11), 3356−3369.

(8) Levine, I.; Al-Ashouri, A.; Musiienko, A.; Hempel, H.; Magomedov, A.; Drevilkauskaite, A.; Getautis, V.; Menzel, D.; Hinrichs, K.; Unold, T.; Albrecht, S.; Dittrich, T. Charge Transfer Rates and Electron Trapping at Buried Interfaces of Perovskite Solar Cells. *Joule* **2021**, *5* (11), 2915−2933.

(9) Paniagua, S. A.; Giordano, A. J.; Smith, O. L.; Barlow, S.; Li, H.; Armstrong, N. R.; Pemberton, J. E.; Brédas, J.-L.; Ginger, D.; Marder, S. R. Phosphonic Acids for Interfacial Engineering of Transparent Conductive Oxides. *Chem. Rev.* **2016**, *116* (12), 7117−7158.

(10) Jiang, Q.; Tirawat, R.; Kerner, R. A.; Gaulding, E. A.; Xian, Y.; Wang, X.; Newkirk, J. M.; Yan, Y.; Berry, J. J.; Zhu, K. Towards Linking Lab and Field Lifetimes of Perovskite Solar Cells. *Nature* **2023**, *623* (7986), 313−318.

(11) Park, S. M.; Wei, M.; Lempesis, N.; Yu, W.; Hossain, T.; Agosta, L.; Carnevali, V.; Atapattu, H. R.; Serles, P.; Eickemeyer, F. T.; Shin, H.; Vafaie, M.; Choi, D.; Darabi, K.; Jung, E. D.; Yang, Y.; Kim, D. B.; Zakeeruddin, S. M.; Chen, B.; Amassian, A.; Filleter, T.; Kanatzidis, M. G.; Graham, K. R.; Xiao, L.; Rothlisberger, U.; Grätzel, M.; Sargent, E. H. Low-Loss Contacts on Textured Substrates for Inverted Perovskite Solar Cells. *Nature* **2023**, *624*, 1−3.

(12) Hossain, K.; Kulkarni, A.; Bothra, U.; Klingebiel, B.; Kirchartz, T.; Saliba, M.; Kabra, D. Resolving the Hydrophobicity of the Me-4PACz Hole Transport Layer for Inverted Perovskite Solar Cells with Efficiency > 20%. *ACS Energy Lett.* **2023**, *8* (9), 3860−3867.

(13) Shen, Z.; Huang, Y.; Dong, Y.; Yan, K.; Chen, H.; Li, C.-Z. Precise Synthesis of Advanced Polyarylamines for Efficient Perovskite Solar Cells. *Nat. Mater.* **2025**, *24*, 1−7.

(14) Wu, T.; Zhang, M.; Gao, X.; Shen, H.; Liu, X.; Li, Z.; Xu, J.; Hao, X. Self-Assembled Monolayers for Perovskite Solar Cells: Molecular Design and Chemical Synthesis. *ACS Nano* **2025**, *19* (27), 24508−24535.

(15) Li, D.; Lian, Q.; Du, T.; Ma, R.; Liu, H.; Liang, Q.; Han, Y.; Mi, G.; Peng, O.; Zhang, G.; Peng, W.; Xu, B.; Lu, X.; Liu, K.; Yin, J.; Ren, Z.; Li, G.; Cheng, C. Co-Adsorbed Self-Assembled Monolayer Enables High-Performance Perovskite and Organic Solar Cells. *Nat. Commun.* **2024**, *15* (1), No. 7605.

(16) Guo, R.; Wang, X.; Jia, X.; Guo, X.; Li, J.; Li, Z.; Sun, K.; Jiang, X.; Alvianto, E.; Shi, Z.; Schwartzkopf, M.; Müller-Buschbaum, P.; Hou, Y. Refining the Substrate Surface Morphology for Achieving Efficient Inverted Perovskite Solar Cells. *Adv. Energy Mater.* **2023**, *13* (43), No. 2302280.

(17) Zheng, X.; Li, Z.; Zhang, Y.; Chen, M.; Liu, T.; Xiao, C.; Gao, D.; Patel, J. B.; Kuciauskas, D.; Magomedov, A.; Scheidt, R. A.; Wang,

X.; Harvey, S. P.; Dai, Z.; Zhang, C.; Morales, D.; Pruett, H.; Wieliczka, B. M.; Kirmani, A. R.; Padture, N. P.; Graham, K. R.; Yan, Y.; Nazeeruddin, M. K.; McGehee, M. D.; Zhu, Z.; Luther, J. M. Co-Deposition of Hole-Selective Contact and Absorber for Improving the Processability of Perovskite Solar Cells. *Nat. Energy* **2023**, *8* (5), 462−472.
(18) Tan, Q.; Li, Z.; Luo, G.; Zhang, X.; Che, B.; Chen, G.; Gao, H.; He, D.; Ma, G.; Wang, J.; Xiu, J.; Yi, H.; Chen, T.; He, Z. Inverted Perovskite Solar Cells Using Dimethylacridine-Based Dopants. *Nature* **2023**, *620* (7974), 545−551.
(19) Gao, D.; Li, B.; Sun, X.; Liu, Q.; Zhang, C.; Qian, L.; Yu, Z.; Li, X.; Wu, X.; Liu, B.; Wang, N.; Vanin, F.; Xia, X.; Gong, J.; Li, N.; Zeng, X. C.; Li, Z.; Zhu, Z. High-Efficiency Perovskite Solar Cells Enabled by Suppressing Intermolecular Aggregation in Hole-Selective Contacts. *Nat. Photonics* **2025**, *19*, 1−8.
(20) Nie, Z.; Meng, W.; Peng, S.; Huang, Y.; Wang, G.; Wang, D.; Sun, X.; Cai, Q.; Wu, B.; Zhou, G.; Xing, G.; Xu, J.; Long, M. Molecular Hybrid Bridging for Efficient and Stable Inverted Perovskite Solar Cells without a Pre-Deposited Hole Transporting Layer *Adv. Mater.* 2025e10685.
(21) Tomita, D.; Ishikawa, R. One-Step Co-Fabrication of Tripod Self-Organized Hole Transport and Perovskite Layers for Perovskite Solar Cells. *Org. Electron.* **2025**, *145*, No. 107296.
(22) Su, Z.; Yu, B.; Sun, Y.; Zhang, J.; Yu, H. Low Temperature Processing of Hole Transport Layer-Free CsPbI2Br Solar Cells Assisted by SAM Co-Deposition. *Appl. Phys. Lett.* **2024**, *125* (24), No. 243902.
(23) Jing, J.; Dong, S.; Zhang, K.; Xie, B.; Zhang, J.; Song, Y.; Huang, F. In-Situ Self-Organized Anode Interlayer Enables Organic Solar Cells with Simultaneously Simplified Processing and Greatly Improved Efficiency to 17.8%. *Nano Energy* **2022**, *93*, No. 106814.
(24) Krausch, G. Surface Induced Self Assembly in Thin Polymer Films. *Mater. Sci. Eng., R* **1995**, *14* (1), 1−94.
(25) Chang, X.; Zhong, J.-X.; Yang, G.; Tan, Y.; Gong, L.; Ni, X.; Ji, Y.; Li, Y.; Zhang, G.; Zheng, Y.; Shao, Y.; Zhou, J.; Yang, Z.; Wang, L.; Wu, W.-Q. Targeted Passivation and Optimized Interfacial Carrier Dynamics Improving the Efficiency and Stability of Hole Transport Layer-Free Narrow-Bandgap Perovskite Solar Cells. *Sci. Bull.* **2023**, *68* (12), 1271−1282.
(26) Chen, S.; Xiao, X.; Chen, B.; Kelly, L. L.; Zhao, J.; Lin, Y.; Toney, M. F.; Huang, J. Crystallization in One-Step Solution Deposition of Perovskite Films: Upward or Downward? *Sci. Adv.* **2021**, *7* (4), No. eabb2412.
(27) Li, C.; Xu, F.; Li, Y.; Li, N.; Yu, H.; Yuanb, B.; Chen, Z.; Li, L.; Cao, B. An Ultrahigh 84.3% Fill Factor for Efficient CH3NH3PbI3 P-i-N Perovskite Film Solar Cell. *Sol. Energy* **2022**, *233*, 271−277.
(28) Zhang, N.; Zhang, Z.; Liu, T.; He, T.; Liu, P.; Li, J.; Yang, F.; Song, G.; Liu, Z.; Yuan, M. Efficient and Stable MAPbI3 Perovskite Solar Cells via Green Anti-Solvent Diethyl Carbonate. *Org. Electron.* **2023**, *113*, No. 106709.
(29) Huang, Y.; Yan, K.; Wang, X.; Li, B.; Niu, B.; Yan, M.; Shen, Z.; Zhou, K.; Fang, Y.; Yu, X.; Chen, H.; Zhang, L.; Li, C.-Z. High-Efficiency Inverted Perovskite Solar Cells via In Situ Passivation Directed Crystallization. *Adv. Mater.* **2024**, *36* (41), No. 2408101.
(30) Zhou, L.; Yan, M.; Luo, G.; Xu, L.; Fang, Y.; Yang, D. Self-Assembled Molecule Doping Enables High-Efficiency Hole-Transport-Layer-Free Perovskite Light-Emitting Diodes. *Adv. Funct. Mater.* **2023**, *33* (36), No. 2303370.
(31) Hutter, E. M.; Gélvez-Rueda, M. C.; Osherov, A.; Bulović, V.; Grozema, F. C.; Stranks, S. D.; Savenije, T. J. Direct−Indirect Character of the Bandgap in Methylammonium Lead Iodide Perovskite. *Nat. Mater.* **2017**, *16* (1), 115−120.
(32) Stranks, S. D.; Burlakov, V. M.; Leijtens, T.; Ball, J. M.; Goriely, A.; Snaith, H. J. Recombination Kinetics in Organic-Inorganic Perovskites: Excitons, Free Charge, and Subgap States. *Phys. Rev. Appl.* **2014**, *2* (3), No. 034007.
(33) Hutter, E. M.; Hofman, J.-J.; Petrus, M. L.; Moes, M.; Abellón, R. D.; Docampo, P.; Savenije, T. J. Charge Transfer from Methylammonium Lead Iodide Perovskite to Organic Transport Materials: Efficiencies, Transfer Rates, and Interfacial Recombination. *Adv. Energy Mater.* **2017**, *7* (13), No. 1602349.
(34) Zhang, X.; Wang, Y.; Zhang, K.; Tao, M.; Guo, H.; Guo, L.; Song, Z.; Wen, J.; Yang, Y.; Hou, Y.; Song, Y. Reinforcing Coverage of Self-Assembled Monomolecular Layers for Inverted Perovskite Solar Cells with Efficiency of 25.70%. *Angew. Chem., Int. Ed.* **2025**, *64*, No. e202423827.
(35) Tang, H.; Shen, Z.; Shen, Y.; Yan, G.; Wang, Y.; Han, Q.; Han, L. Reinforcing Self-Assembly of Hole Transport Molecules for Stable Inverted Perovskite Solar Cells. *Science* **2024**, *383* (6688), 1236−1240.
(36) Shard, A. G.; Clifford, C. A. Summary of ISO/TC 201 Standard: ISO 19668—Surface Chemical Analysis—X-Ray Photoelectron Spectroscopy—Estimating and Reporting Detection Limits for Elements in Homogeneous Materials. *Surf. Interface Anal.* **2018**, *50* (1), 87−89.
(37) Lee, T.-W. Over a Decade of Progress in Metal-Halide Perovskite Light-Emitting Diodes. *Adv. Mater.* **2025**, *37* (25), No. 2508542.
(38) Huang, C.; Fu, W.; Li, C.-Z.; Zhang, Z.; Qiu, W.; Shi, M.; Heremans, P.; Jen, A. K.-Y.; Chen, H. Dopant-Free Hole-Transporting Material with a C3h Symmetrical Truxene Core for Highly Efficient Perovskite Solar Cells. *J. Am. Chem. Soc.* **2016**, *138* (8), 2528−2531.
(39) Xiong, W.; Zou, C.; Tang, W.; Xing, S.; Wang, Z.; Zhao, B.; Di, D. Efficient and Bright Blue Perovskite LEDs Enabled by a Carbazole-Phosphonic Acid Interface. *ACS Energy Lett.* **2023**, *8* (7), 2897−2903.
(40) Shen, G.; Zhang, Y.; Juarez, J.; Contreras, H.; Sindt, C.; Xu, Y.; Kline, J.; Barlow, S.; Reichmanis, E.; Marder, S. R.; Ginger, D. S. Increased Brightness and Reduced Efficiency Droop in Perovskite Quantum Dot Light-Emitting Diodes Using Carbazole-Based Phosphonic Acid Interface Modifiers. *ACS Nano* **2025**, *19* (1), 1116−1127.
(41) Fernández Garrillo, P. A.; Grévin, B.; Chevalier, N.; Borowik, Ł. Calibrated Work Function Mapping by Kelvin Probe Force Microscopy. *Rev. Sci. Instrum.* **2018**, *89* (4), No. 043702.
(42) Peng, W.; Zhang, Y.; Zhou, X.; Wu, J.; Wang, D.; Qu, G.; Zeng, J.; Xu, Y.; Jiang, B.; Zhu, P.; Du, Y.; Li, Z.; Lei, X.; Liu, Z.; Yan, L.; Wang, X.; Xu, B. A Versatile Energy-Level-Tunable Hole-Transport Layer for Multi-Composition Inverted Perovskite Solar Cells. *Energy Environ. Sci.* **2025**, *18* (2), 874−883.
(43) Khan, Md. Z. H. Effect of ITO Surface Properties on SAM Modification: A Review toward Biosensor Application. *Cogent Eng.* **2016**, *3* (1), No. 1170097.
(44) Kim, D.-H.; Lee, H.-J.; Lee, S.-H.; Kang, Y.-J.; Kwon, S.-N.; Kim, D.-H.; Na, S.-I. Mixed Self-Assembled Hole-Transport Monolayer Enables Simultaneous Improvement of Efficiency and Stability of Perovskite Solar Cells. *Sol. RRL* **2024**, *8* (9), No. 2400067.
(45) Liu, Z.; Yu, B.; Shi, S.; Yu, H. Optimizing Monolayers for High-Efficiency Methylammonium-Free Perovskite Solar Cells. *ACS Appl. Mater. Interfaces* **2025**, *17* (13), 19838−19847.
(46) Guo, Y.; Huang, L.; Wang, C.; Huang, J.; Liu, S.; Liu, X.; Zhang, J.; Hu, Z.; Zhu, Y. Efficient Inverted Perovskite Solar Cells with a Low-Temperature Processed NiOx/SAM Hole Transport Layer. *J. Mater. Chem. C* **2024**, *12* (4), 1507−1515.
(47) Liu, S.-C.; Lin, H.-Y.; Hsu, S.-E.; Wu, D.-T.; Sathasivam, S.; Daboczi, M.; Hsieh, H.-J.; Zeng, C.-S.; Hsu, T.-G.; Eslava, S.; J Macdonald, T.; Lin, C.-T. Highly Reproducible Self-Assembled Monolayer Based Perovskite Solar Cells via Amphiphilic Polyelectrolyte. *J. Mater. Chem. A* **2024**, *12* (5), 2856−2866.
(48) Xu, D.; Wu, P.; Tan, H. Self-Assembled Monolayers for Perovskite Solar Cells. *Inf. Funct. Mater.* **2024**, *1* (1), 2−25.
(49) Jeon, N. J.; Noh, J. H.; Kim, Y. C.; Yang, W. S.; Ryu, S.; Seok, S. I. Solvent Engineering for High-Performance Inorganic−Organic Hybrid Perovskite Solar Cells. *Nat. Mater.* **2014**, *13* (9), 897−903.
(50) Deng, Y.; Van Brackle, C. H.; Dai, X.; Zhao, J.; Chen, B.; Huang, J. Tailoring Solvent Coordination for High-Speed, Room-Temperature Blading of Perovskite Photovoltaic Films. *Sci. Adv.* **2019**, *5* (12), No. eaax7537.

(51) Zhang, F.; Song, J.; Zhang, L.; Niu, F.; Hao, Y.; Zeng, P.; Niu, H.; Huang, J.; Lian, J. Film-through Large Perovskite Grains Formation via a Combination of Sequential Thermal and Solvent Treatment. *J. Mater. Chem. A* **2016**, *4* (22), 8554−8561.
(52) Tu, Y.; Wu, J.; Lan, Z.; He, X.; Dong, J.; Jia, J.; Guo, P.; Lin, J.; Huang, M.; Huang, Y. Modulated CH3NH3PbI3−xBrx Film for Efficient Perovskite Solar Cells Exceeding 18%. *Sci. Rep.* **2017**, *7* (1), No. 44603.
(53) Liu, T.; Zong, Y.; Zhou, Y.; Yang, M.; Li, Z.; Game, O. S.; Zhu, K.; Zhu, R.; Gong, Q.; Padture, N. P. High-Performance Formamidinium-Based Perovskite Solar Cells via Microstructure-Mediated δ-to-α Phase Transformation. *Chem. Mater.* **2017**, *29* (7), 3246−3250.
(54) Zhang, X.; Han, D.; Chen, X. Effects of Solvent Coordination on Perovskite Crystallization. *Acta Phys.-Chim. Sin.* **2020**, *37* (4), No. 2008055.
(55) Hansen, C. M. *Hansen Solubility Parameters: A User's Handbook*, 2nd ed.; CRC Press: Boca Raton, 2007 DOI: 10.1201/9781420006834.
(56) Vasudevan, V.; Mushrif, S. H. Force Field Parameters for N,N-Dimethylformamide (DMF) Revisited: Improved Prediction of Bulk Properties and Complete Miscibility in Water. *J. Mol. Liq.* **2015**, *206*, 338−342.
(57) Basma, N.; Cullen, P. L.; Clancy, A. J.; Shaffer, M. S. P.; Skipper, N. T.; Headen, T. F.; Howard, C. A. The Liquid Structure of the Solvents Dimethylformamide (DMF) and Dimethylacetamide (DMA). *Mol. Phys.* **2019**, *117* (22), 3353−3363.
(58) Brayton, C. F. Dimethyl Sulfoxide (DMSO): A Review. *Cornell Vet.* **1986**, *76* (1), 61−90.
(59) Pope, D. C.; Oliver, W. T. Dimethyl Sulfoxide (DMSO). *Can. J. Comp. Med. Vet. Sci.* **1966**, *30* (1), 3−8.
(60) MacGregor, W. S. The Chemical and Physical Properties of Dmso. *Ann. N.Y. Acad. Sci.* **1967**, *141* (1), 3−12.
(61) Ulman, A. Formation and Structure of Self-Assembled Monolayers. *Chem. Rev.* **1996**, *96* (4), 1533−1554.
(62) Schwartz, D. K. Mechanisms and Kinetics of Self-assembled Monolayer Formation. *Annu. Rev. Phys. Chem.* **2001**, *52*, 107−137.
(63) Prashar, D. Self Assembled Monolayers -A Review.
(64) Yang, Y.; Liu, M.; Gai, S.; Liu, X.; Wang, Y.; Yu, Y.; Zhang, B.; Xia, J.; Rashid bin Mohd Yusoff, Abd.; Zhang, Y. Design and Applications of Hole-Selective Self-Assembled Monolayers for Perovskite Photovoltaics. *Chem. Eng. J.* **2025**, *504*, No. 158870.
(65) Lee, K. C.; Kim, S.; Son, J.; Kong, J.; Yang, C. A Brief Review on Self-Assembled Monolayers in Organic Solar Cells: Progress, Challenges, and Future Prospects. *ACS Appl. Electron. Mater.* **2025**, *7* (3), 946−963.
(66) Murray, J. S.; Sen, K. *Molecular Electrostatic Potentials: Concepts and Applications*; Elsevier, 1996.
(67) Zhao, J.; Caselli, V. M.; Bus, M.; Boshuizen, B.; Savenije, T. J. How Deep Hole Traps Affect the Charge Dynamics and Collection in Bare and Bilayers of Methylammonium Lead Bromide. *ACS Appl. Mater. Interfaces* **2021**, *13* (14), 16309−16316.
(68) SCM. Documentation. https://www.scm.com/doc/ (accessed Aug 28, 2025).
(69) Pye, C. C.; Ziegler, T. An Implementation of the Conductor-like Screening Model of Solvation within the Amsterdam Density Functional Package. *Theor. Chem. Acc.* **1999**, *101* (6), 396−408.

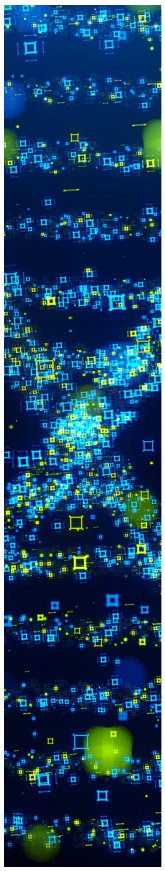

https://doi.org/10.1021/acsami.5c18266
ACS Appl. Mater. Interfaces 2025, 17, 67306−67317